

# Heteroatom-Substituted Delaminated Zeolites as Solid Lewis Acid Catalysts

Xiaoying Ouyang,<sup>†</sup> Son-Jong Hwang,<sup>‡</sup> Dan Xie,<sup>§</sup> Thomas Rea,<sup>§</sup> Stacey I. Zones,<sup>\*,†,§</sup> and Alexander Katz<sup>\*,†</sup>

<sup>†</sup>Department of Chemical and Biomolecular Engineering, University of California at Berkeley, Berkeley, California 94720, United States

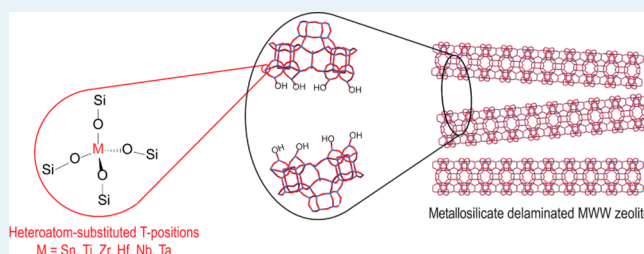
<sup>‡</sup>Department of Chemical Engineering, California Institute of Technology, Pasadena, California 91125, United States

<sup>§</sup>Chevron Energy Technology Company, Richmond, California 94804, United States

## S Supporting Information

**ABSTRACT:** This manuscript represents a comparative study of Lewis acid catalysis using heteroatom-substituted delaminated zeolites, which are synthesized using an approach that obviates the need for surfactants and sonication during exfoliation. The comparison involves heteroatom substitution into silanol nests of delaminated zeolites consisting of DZ-1 and deboronated UCB-4. Diffuse reflectance ultraviolet (DR-UV) spectroscopy demonstrates framework heteroatom sites, and the Lewis acidity of these sites is confirmed using infrared spectroscopy of adsorbed pyridine. The enhanced catalytic accessibility of these Lewis acid sites is confirmed when performing Baeyer–Villiger oxidation of substituted 2-adamantanones with hydrogen peroxide as the oxidant. Comparison of delaminated Sn-DZ-1 with three-dimensional Sn-Beta for this reaction shows that the delaminated zeolite is more active for bulkier ketone substrates. The role of the two-dimensional crystalline framework of the delaminated zeolite on catalysis is highlighted by comparing delaminated zeolites Sn-DZ-1 with Sn-UCB-4. The former exhibits a significantly higher activity for Baeyer–Villiger oxidation, yet when comparing Ti-DZ-1 with Ti-UCB-4, it is the latter that exhibits a significantly higher activity for olefin epoxidation with organic hydrogen peroxide, whereas both delaminated zeolites are more robust and selective in epoxidation catalysis compared with amorphous Ti/SiO<sub>2</sub>.

**KEYWORDS:** delaminated zeolites, silanol nest, heteroatom substitution, Lewis acid catalysis, Baeyer–Villiger oxidation, epoxidation



## INTRODUCTION

Zeolites are microporous crystalline materials that continue to attract increasing attention in catalysis because of their tunable catalytic properties and shape selectivities associated with well-defined heteroatom-containing active sites, which are located within uniform environments as defined by the framework (i.e., micropores, channels, and channel intersections). Isomorphous substitution of framework tetravalent heteroatoms (e.g., Ti, Zr, Sn, etc.) and pentavalent heteroatoms (e.g., Ta, Nb, V, etc.) for framework Si leads to zeolite-based solid Lewis acid catalysts. Such solids form acid–base adducts by accepting electrons in the empty orbitals of the heteroatoms from either a reactant or an oxidizing agent. They have been used extensively, in the case of Ti-containing zeolites<sup>1–3</sup> for example, in oxidation reactions of alcohols and alkanes, olefin epoxidation, hydroxylation of aromatics, and cyclohexanone ammoxidation.<sup>4–6</sup> In addition, a variety of substituted frameworks have been employed for hosting Ti via its direct incorporation during synthesis, such as Ti-Beta,<sup>7</sup> Ti-ZSM-48,<sup>8</sup> Ti-SSZ-33,<sup>9</sup> and Ti-MWW,<sup>10</sup> among many others. In addition, Sn and Zr have been incorporated into tetrahedral framework sites of zeolite Beta, and the resulting materials have been found promising for several types of Lewis acid-catalyzed reactions, including, for Sn-Beta, Baeyer–Villiger

oxidation,<sup>11,12</sup> and isomerization of sugars,<sup>13–15</sup> whereas Zr-Beta is active for Meerwein–Ponndorf–Verley (MPV) reduction and synthesis of terephthalic acid via Diels–Alder reactions with ethylene and oxidized variants of 5-hydroxymethylfurfural.<sup>16</sup>

However, in general, the small pore size of zeolites restricts their usefulness in many catalytic applications involving larger molecules. To expand the scope of zeolite-based catalysis, there has been an emergence of approaches for synthesis of delaminated zeolites. Using previously described delaminated borosilicates consisting of DZ-1<sup>17</sup> and UCB-4,<sup>18</sup> here, in this manuscript, we describe heteroatom substitution into deboronated and delaminated zeolites having MWW and SSZ-70 framework topologies, respectively, and compare the use of these solid catalysts for Lewis acid-catalyzed reactions.

It is relevant to briefly contrast the previously described syntheses of delaminated zeolites DZ-1 and UCB-4. The synthesis of DZ-1 is accomplished by permanently disrupting (i.e., this disruption persists even after calcination of the material at 550 °C) interlayer hydrogen bonding via aqueous Zn(NO<sub>3</sub>)<sub>2</sub>

**Received:** December 21, 2014

**Revised:** March 27, 2015

**Published:** April 1, 2015

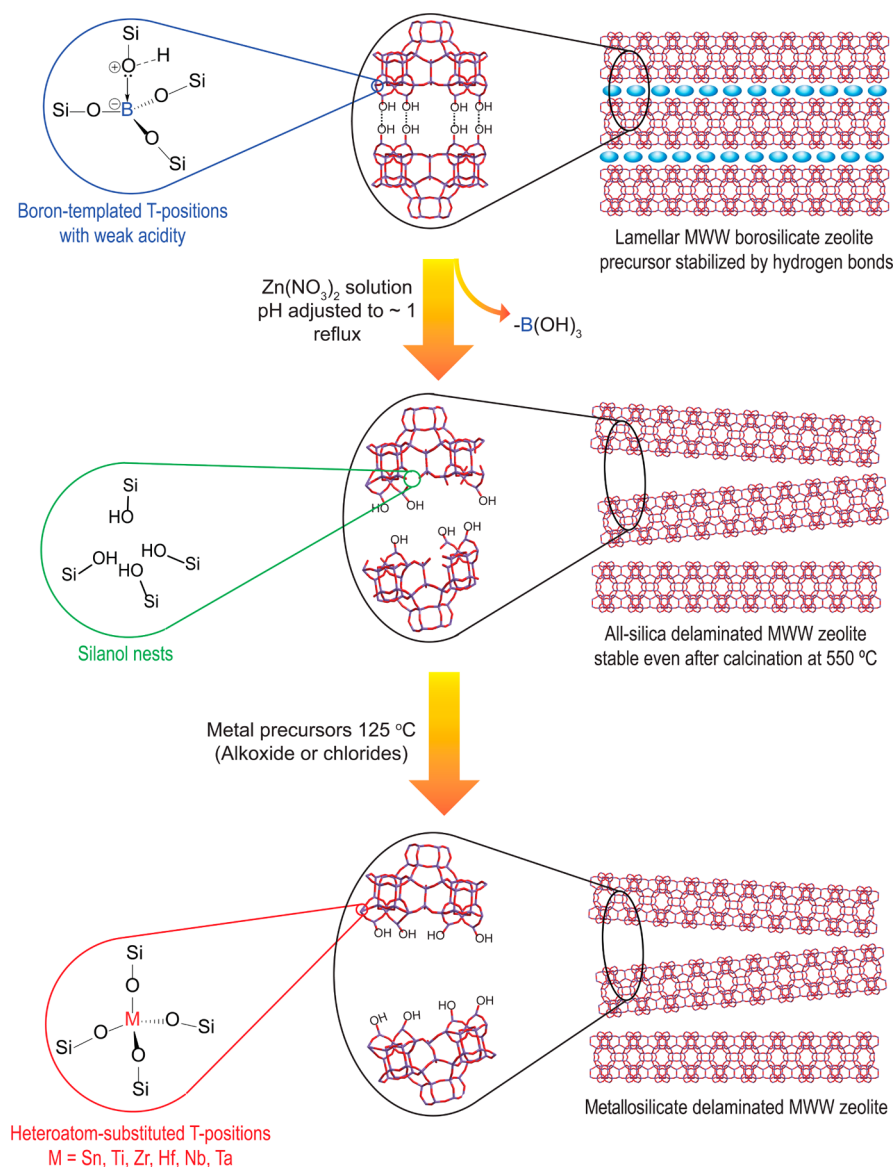


**Figure 1.** Schematic diagram of the surfactant-free exfoliation of a MWW-type borosilicate zeolite precursor into a delaminated zeolite consisting of high density of silanol nests and the reoccupation of the silanol nests with various heteroatoms.

treatment of ERB-1P (Si/B = 11), as shown in Figure 1.<sup>17</sup> We previously demonstrated this to be accompanied by (i) loss of framework B (Si/B = 73 in DZ-1) as a result of the mildly acidic aqueous solvent, (ii) generation of silanol<sup>19,20</sup> nests<sup>16,17</sup> in framework T-site locations previously occupied by B, and (iii) extraction of piperidine (PI) during delamination. We believe that, similar to our previous  $\text{Al}(\text{NO}_3)_3$ -induced delamination method,<sup>21</sup> delamination is facilitated by lattice distortions along both the *c*-axis and the *a*-*b* plane, which occur concomitantly with silanol nest formation. We further hypothesized that, on the basis of precedent in three-dimensional zeolites,<sup>9,10</sup> those silanol nests that are located within 12-MR near the external surface should be accessible for heteroatom substitution with metal precursors.

Though crystallographically distinct from ERB-1, B-SSZ-70 has several structural features that are similar to MWW-type zeolites (e.g., ERB-1, MCM-22, SSZ-25, etc.), in that it is also synthesized through an isolable layered-zeolite precursor, which consists of lamellae.<sup>22,23</sup> Yet in contrast to DZ-1, there is no deboronation during synthesis of UCB-4 from B-SSZ-70, as

facilitated by the nonaqueous solvent and mild delamination conditions.<sup>18</sup> Although we previously attempted to synthesize a Ti-containing delaminated SSZ-70 via direct Ti incorporation during materials synthesis and achieved isolated Ti sites within a siliceous zeolite framework, the resulting materials failed to show catalytic activity when using either organic hydroperoxide or hydrogen peroxide as oxidants.<sup>18</sup> Here, in this manuscript, we use a different method of heteroatom incorporation into the SSZ-70-based delaminated zeolite. This method involves initial deboronation of calcined UCB-4, which synthesizes a UCB-4 with Si/B =  $\infty$ , as shown in Figure 2. Like DZ-1, deboronated UCB-4 also contains a high density of silanol nests, some of which are located within 12-MR near the external surface.

In both DZ-1 and deboronated UCB-4, we synthesize heteroatom-substituted delaminated zeolite catalysts by reacting a metal precursor with a deboronated delaminated zeolite via condensation of silanol nests with the precursor. The relevant precedent in this regard is synthesis of Ti-SSZ-33 by reacting  $\text{TiCl}_4$  vapor with silanol nests,<sup>9</sup> our recent synthesis of Ti-DZ-1,<sup>17</sup> and the synthesis of a delaminated Ti-MWW material.<sup>24</sup> The

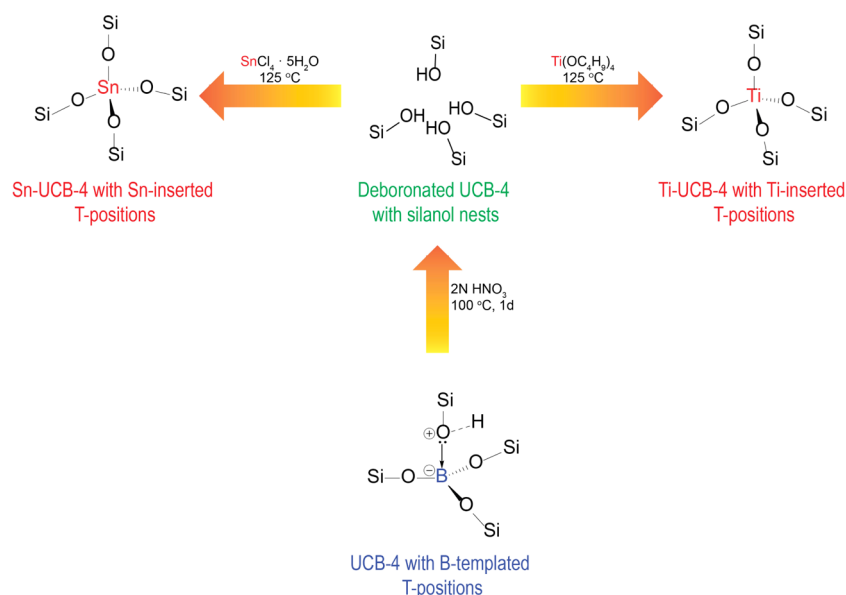


**Figure 2.** Schematic diagram of the preparation of Sn-UCB-4 and Ti-UCB-4. (See Figure 1 for the description of how the sites are located in larger lamellae in the zeolite framework.)

latter is a nice demonstration of synthesis involving deboronation and metallation; however, it requires the use of a high pH, organic surfactant, and sonication for achieving exfoliation, in stark contrast to Ti-DZ-1, which requires none of these. Another crucial differentiating aspect between the delaminated Ti-MWW and Ti-DZ-1 materials is that the delaminated Ti-MWW material consists of Ti sites throughout the bulk of the material, rather than just near the external surface (i.e., within 12-MR), as in Ti-DZ-1 and all of the heteroatom-substituted materials described in this manuscript.<sup>24</sup>

We investigate the role of both metal and framework connectivity in controlling catalysis with solid Lewis acids, using relevant model reactions consisting of Baeyer–Villiger oxidation and olefin epoxidation with organic hydroperoxide as oxidant. These catalysts consist of sites that are near the external surface and, as a result, in a half-open environment to their solvent-fluid surroundings, compared with conventional heteroatom sites within three-dimensional zeolites, which are buried within internal micropores. Thus, our results inform on the relationship between structure and function while reinforcing the advantages of these heteroatom-substituted zeolitic materials over their amorphous counterparts as well as the catalytic role of the zeolitic framework in these open active sites.

## EXPERIMENTAL SECTION

**Materials.** All reagents in this manuscript were reagent-grade quality and were used as received unless otherwise noted. Syntheses of ERB-1P, ERB-1C (calcined ERB-1P), DZ-1, and Ti-DZ-1 were performed as described previously,<sup>17</sup> as were syntheses of materials B-SSZ-70 precursor and UCB-4.<sup>18</sup>

**Synthesis of Sn-DZ-1.** A 4 g portion of SnCl<sub>4</sub>·5H<sub>2</sub>O was added to 1 g of DZ-1 in a sealed, thick-walled glass reactor at room temperature in a glovebox. A viscous slurry formed after heating this solid mixture to 125 °C under vigorous stirring with a magnetic stir bar. After 1 h (the Sn content within the final material could be adjusted by varying the reaction time at this step between 5 min and 3 h), 20 mL of *n*-BuOH was added into the slurry, and stirring continued for an additional 10 min. The solid product was collected on a filter; washed thoroughly with *n*-

BuOH, followed by acetone to remove residual SnCl<sub>4</sub> and weakly anchored Sn species; and finally, air-dried. The resulting material was denoted as Sn-DZ-1.

### Syntheses of Zr-DZ-1, Hf-DZ-1, Nb-DZ-1, and Ta-DZ-1.

For synthesis of Zr-DZ-1, 4 g Zr(OC<sub>4</sub>H<sub>9</sub>)<sub>4</sub> was added to 1 g of DZ-1, and the resulting viscous slurry was heated in a sealed, thick-walled glass reactor at 150 °C and vigorously stirred with a stir bar for 1 h. The temperature was lowered to 120 °C, and 20 mL of *n*-BuOH was added to the slurry, after which stirring continued for 10 min. The solid product was collected on a filter; washed thoroughly with *n*-BuOH, followed by acetone to remove residual Zr(OC<sub>4</sub>H<sub>9</sub>)<sub>4</sub> and surface-grafted Zr species; and finally, air-dried. The resulting material was denoted as Zr-DZ-1. Similar procedures were followed for synthesis of Hf-DZ-1, Nb-DZ-1, and Ta-DZ-1, except that Hf(OC<sub>4</sub>H<sub>9</sub>)<sub>4</sub>, Nb(OC<sub>2</sub>H<sub>5</sub>)<sub>5</sub>, or Ta(OC<sub>2</sub>H<sub>5</sub>)<sub>5</sub>, respectively, was used instead of Zr(OC<sub>4</sub>H<sub>9</sub>)<sub>4</sub>.

**Synthesis of Deboronated UCB-4.** A 20 mL portion of 2.0 N HNO<sub>3</sub> solution was added to 0.50 g of the as-made UCB-4 in a sealed, thick-walled glass reactor and stirred at 100 °C for 24 h. The solid product was collected on a filter, washed thoroughly with deionized water, and then air-dried.

**Synthesis of Sn-UCB-4 and Ti-UCB-4.** A 4 g portion of SnCl<sub>4</sub>·5H<sub>2</sub>O was added to 1 g of deboronated UCB-4 in a sealed, thick-walled glass reactor at room temperature. The viscous slurry mixture was heated at 125 °C under vigorous stirring with a magnetic stir bar. After 1 h, 20 mL of *n*-BuOH was added to the slurry, after which time stirring continued for an additional 10 min. Subsequently, the solid product was collected on a filter; washed thoroughly with *n*-BuOH and acetone to remove residual SnCl<sub>4</sub> and surface-grafted Sn species; and finally, air-dried. The resulting material is denoted as Sn-UCB-4. Similar procedures were followed for synthesis of Ti-UCB-4, except that the same weight of Ti(OC<sub>2</sub>H<sub>5</sub>)<sub>4</sub> was used instead of SnCl<sub>4</sub>·5H<sub>2</sub>O.

## CHARACTERIZATION TECHNIQUES

**ICP–MS.** The Si and Al contents of all materials were determined using inductively coupled plasma mass spectroscopy (ICP–MS) analysis conducted at Galbraith Laboratories, USA.

Table 1. Synthesis Conditions and Physicochemical Properties of DZ-1 Related Materials

sample <sup>a</sup>	heteroatom (M)	metal precursor	Si/M ratio	Si/B ratio	$V_{\text{micro}}^d$ (cm <sup>3</sup> /g)	$V_{\text{meso}}^e$ (cm <sup>3</sup> /g)	$S_{\text{ext}}^f$ (m <sup>2</sup> /g)
ERB-1C	B	n/a	n/a	10	0.12	0.04	53
UCB-4	B	n/a	n/a	30	0.12	0.08	96
DZ-1	n/a	n/a	n/a <sup>b</sup>	>200	0.08	0.10	131
Sn-DZ-1	Sn	SnCl <sub>4</sub> ·5H <sub>2</sub> O	65 <sup>c</sup>	>200	0.05	0.12	148
Ti-DZ-1	Ti	Ti(OC <sub>4</sub> H <sub>9</sub> ) <sub>4</sub>	67	>200	0.04	0.14	171
Zr-DZ-1	Zr	Zr(OC <sub>4</sub> H <sub>9</sub> ) <sub>4</sub>	57	>200	0.05	0.12	145
Hf-DZ-1	Hf	Hf(OC <sub>4</sub> H <sub>9</sub> ) <sub>4</sub>	62	>200	0.05	0.12	150
Nb-DZ-1	Nb	Nb(OC <sub>2</sub> H <sub>5</sub> ) <sub>5</sub>	40	>200	0.04	0.13	165
Ta-DZ-1	Ta	Ta(OC <sub>2</sub> H <sub>5</sub> ) <sub>5</sub>	39	>200	0.04	0.14	170
Sn-UCB-4	Sn	SnCl <sub>4</sub> ·5H <sub>2</sub> O	100	>200	0.14	0.09	97
Ti-UCB-4	Ti	Ti(OC <sub>4</sub> H <sub>9</sub> ) <sub>4</sub>	88	>200	0.14	0.08	90

<sup>a</sup>All the samples in Table 1 are calcined materials. <sup>b</sup>The Si/Zn ratio for DZ-1 is >200. <sup>c</sup>Sn-DZ-1 can be synthesized with different Sn contents, e.g., Si/Sn = 65 and 94, respectively. <sup>d</sup>Micropore volume determined by *t*-plot method. <sup>e</sup>Mesopore (between 1 and 10 nm in diameter) volume determined by NLDFT method. <sup>f</sup>External surface area determined by *t*-plot method.

**TEM.** Transmission electron microscopy (TEM) images were recorded on a JEOL JEM-2010 electron microscope (200 kV) at Chevron Energy Technology Company.

**N<sub>2</sub> Physisorption.** Nitrogen physisorption isotherms were measured on a Micromeritics ASAP2020 instrument at 77 K. Prior to measurement, samples were evacuated at 350 °C for 4 h. The pore-size distributions were calculated by the nonlocal density functional (NLDFT) method<sup>25</sup> on the basis of measured nitrogen adsorption data.

**FTIR.** Infrared spectra of self-supported zeolite pellets were recorded using a Nicolet 6700 FTIR spectrometer at 2 cm<sup>-1</sup> resolution. Prior to measurement, zeolite pellets were first activated at 500 °C in vacuo for 2 h. The background spectrum, recorded under identical operating conditions except in the absence of a sample in the cell, was always automatically subtracted from measured spectra. For studying acid sites, the zeolite pellets were exposed to pyridine vapor for ~5 min at 25 °C. Spectra were subsequently recorded after evacuation for 1 h at 150 °C (3 °C/min ramp rate from 25 °C).

**DR-UV.** Diffuse reflectance UV–vis spectra were collected using a Cary 4000 UV–vis spectrophotometer. Poly-(tetrafluoroethylene) powder (Aldrich) was used for baseline correction.

**Baeyer–Villiger (BV) Oxidation.** The BV reactions were performed on the DZ-1-based materials using the following reaction conditions: catalyst, 0.66 mol % of metal with respect to ketone; ketone, 1 mmol; H<sub>2</sub>O<sub>2</sub>, 1.5 mmol; dioxane, 3 mL; temperature, 75 °C. Dodecane was used as an internal standard. The reactions were performed in a 15 mL sealed, thick-walled glass reactor with vigorous stirring. Aliquots from the reaction mixture were sampled and analyzed by gas chromatography (FID detector) using an Agilent 6890 and a 30-m HP-1 column. The lactone products were identified by comparing their retention times. The conversion was calculated on the basis of the total initial amount of ketone.

**Olefin Epoxidation.** Cyclohexene was purified by passage through a column of Al<sub>2</sub>O<sub>3</sub> immediately before use. 1-Octene was purified by distillation and then stored with molecular sieves 3A in a Schlenk tube. *n*-Octane was distilled over sodium/benzophenone under Ar. Generally, olefin epoxidation rates and selectivities were measured by making a slurry in a 50 mL flask consisting of 25 mg of catalyst, 5.9 mmol of 1-octene, and 20 mL of octane as solvent at 60 °C, to which 0.59 mmol of TBHP (4.9 mol/L in nonane, Aldrich) was added to start the reaction. Olefin epoxidation was also performed under more forcing conditions

consisting of a higher TBHP concentration and temperature. These conditions were the following: 25 mg of catalyst, 3.0 mmol of 1-octene, and 10 mL of octane as solvent were combined to make a slurry at 110 °C, to which 1.5 mmol of TBHP was added. For the case of internal olefin cyclohexene epoxidation, the conditions were thus: 25 mg of catalyst, 5.9 mmol of cyclohexene, and 10 mL of octane as solvent were combined to make a slurry at 60 °C, to which 0.59 mmol of TBHP was added. The reaction temperature was controlled by using a heated oil bath on a hot plate. Liquid aliquots were removed and analyzed for reactants and products by gas chromatography (Agilent 6890, HP-1 methylsilicone capillary column) to measure catalytic reaction rates and selectivities. The selectivities reported represent instantaneous selectivities based on the rates of epoxide formation and organic hydroperoxide consumption at a given time.

## RESULTS AND DISCUSSIONS

**Heteroatom Metal Reinsertion into Deboronated Delaminated Zeolites.** The synthesis of heteroatom-substituted delaminated zeolites based on DZ-1 and UCB-4 and consisting of tetravalent and pentavalent metals, such as Hf, Nb, Ta, Ti, Sn, and Zr, is summarized in Table 1. Generally, these syntheses are accomplished by treating the all-silica delaminated zeolites consisting of either DZ-1 or deboronated UCB-4 with an excess of neat reactive metal precursor (see Table 1) so as to make a slurry, which is stirred at 100–125 °C, prior to a mild wash with *n*-BuOH for removing unreacted precursor and extra-framework metal sites.

**TEM Characterization.** TEM images of the delaminated zeolite DZ-1 and Sn-DZ-1 in Figure 3b and c, respectively, clearly show curved thin layers that lack long-range order, which is consistent with the PXRD data in Figure S1. This is in stark contrast with TEM characterization of ERB-1P, which shows the expected lamellar assembly consisting of rectilinear sheets (Figure 3a) in the precursor material. The morphology of DZ-1 remains preserved even after reoccupation of the silanol nests with Sn and Ti, as shown by data in Figure S3c–f.

**N<sub>2</sub> Physisorption at 77 K.** N<sub>2</sub> adsorption–desorption isotherms of ERB-1C, DZ-1, and Sn-DZ-1 were measured for textural characterization and are shown in Figure 4a, and the pore size distributions derived from the NLDFT model<sup>25</sup> are represented in Figure 4b. Table 1 summarizes the micropore and mesopore volumes as well as external surface areas, as determined by the *t*-plot method. The N<sub>2</sub> physisorption data for

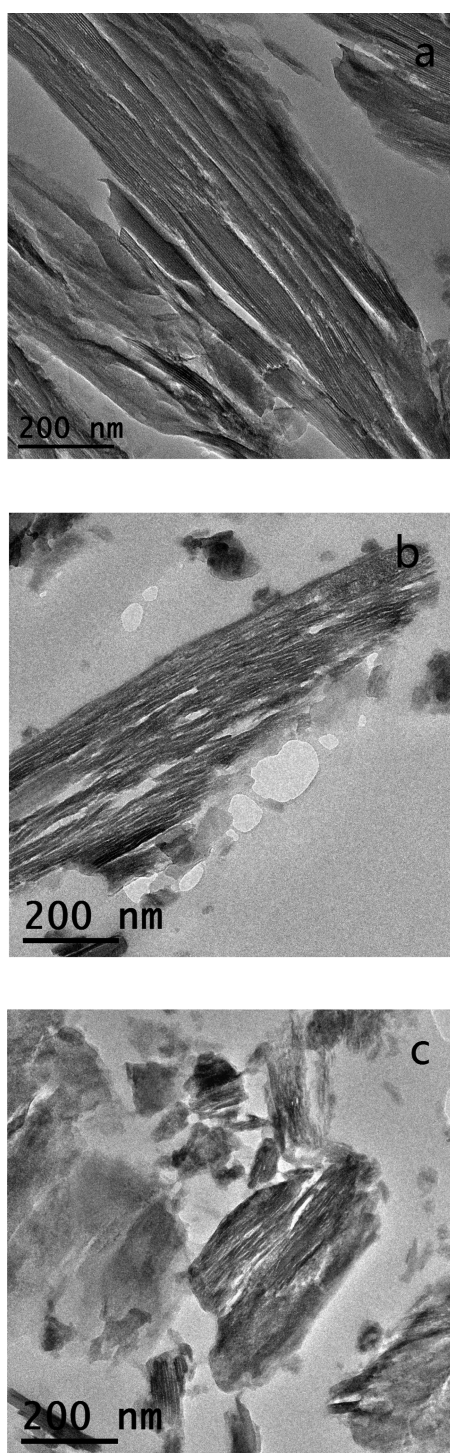


**Figure 3.** TEM images characterizing (a) ERB-1P, (b) DZ-1, and (c) Sn-DZ-1.

DZ-1 is consistent with its delamination, as discussed and shown using PXRD (Figure S1). In particular, the external surface area of DZ-1 is 2.5-fold higher than that of the corresponding calcined 3D zeolite ERB-1C. DZ-1 also exhibits a significantly lower micropore volume and higher mesopore volume relative to ERB-1C, which is interpreted as a disappearance of 10-MR micropores during delamination as well as the gained mesoporosity between delaminated layers.

$N_2$  physisorption data are consistent with preservation of the delaminated morphology of DZ-1 upon heteroatom substitution

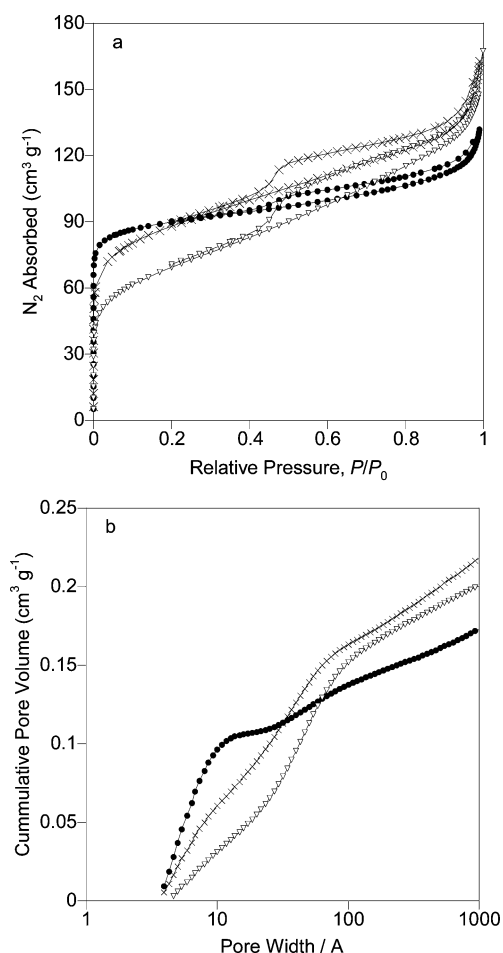


**Figure 4.** (a)  $N_2$  adsorption isotherms and (b)  $N_2$  NLDFT cumulative pore volume plots for ERB-1C (●), calcined DZ-1 (×), and calcined Sn-DZ-1 (∇).

in Sn-DZ-1, which reinforces data from TEM in Figure 3. When compared with DZ-1, Sn-DZ-1 shows a slightly decreased micropore volume ( $0.05 \text{ cm}^3/\text{g}$  for Sn-DZ-1 vs  $0.08 \text{ cm}^3/\text{g}$  for DZ-1), increased mesopore volume ( $0.12 \text{ cm}^3/\text{g}$  for Sn-DZ-1 vs  $0.10 \text{ cm}^3/\text{g}$  for DZ-1), and increased external surface area ( $148 \text{ m}^2/\text{g}$  Sn-DZ-1 vs  $131 \text{ m}^2/\text{g}$  for DZ-1). These slight but consistent and meaningful changes in textural properties relative to DZ-1 are also observed in all other heteroatom-substituted DZ-1 materials consisting of Hf, Ta, Ti, Nb, and Zr heteroatoms in framework positions, as shown in Table 1. This micropore volume reduction and increase in mesopore volume/external surface area may indicate further delamination and layer separation, as promoted by the incorporation of heteroatoms into silanol nests within DZ-1. A hypothesis along these lines is as follows: Data from B-elemental analysis demonstrate that more than 80% of the B is removed during delamination and synthesis of DZ-1. Assuming that each removed B yields a silanol nest, the ratio of Si atoms to silanol nests is estimated to be 10:1 in DZ-1 following delamination. Such a large number of silanol nests as structural defects may cause the delaminated zeolite sheets to become mechanically less strong and, because of flexibility, may lead to the filling of spaces between sheets. Such a decreased mechanical integrity due to the silanol nest would cause a partial collapse of framework structure and eventual loss of external surface area, as we have reported for a case of ERB-1P.<sup>16,23</sup> Once the structural defects consisting of silanol nests of DZ-1 are

healed by insertion of metal heteroatoms into these framework positions, the delaminated zeolite sheets could maintain a higher level of mechanical integrity so as to be able to support further delamination and layer separation without collapse. An alternative explanation would be that the reduction in micropore volume in Table 1 upon metal heteroatom reinsertion is due to some pore blockage by extra-framework heteroatoms. This could be partially substantiated by the lack of closure of both isotherm branches below a  $P/P_0$  of 0.2; however, this in and of itself would not contribute to either the observed increase in mesopore volume or the larger external surface area.

#### Characterization of Acid Sites by Pyridine Adsorption.

The number density and strength of acid sites in DZ-1 and heteroatom-substituted DZ-1 are compared using adsorption of pyridine, and this comparison also includes ERB-1 material ( $\text{Si}/\text{Al} = 15$ ,  $S_{\text{ext}} = 133 \text{ m}^2/\text{g}$ ,  $V_{\text{micro}} = 0.09 \text{ cm}^3/\text{g}$ ),<sup>21</sup> in which aluminum reinsertion accompanies delamination. Relevant FTIR spectra of pyridine-adsorbed materials in the wavelength range of  $1700\text{--}1430 \text{ cm}^{-1}$  are shown in Figure 5. Infrared bands at  $1542$  and

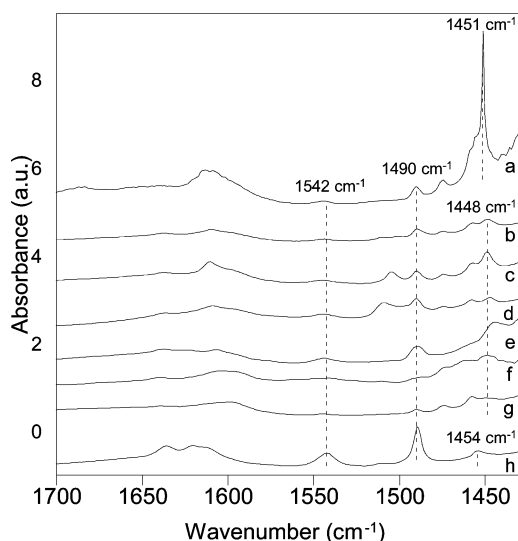


**Figure 5.** FTIR spectra of activated samples (a) Sn-DZ-1, (b) Nb-DZ-1, (c) Ta-DZ-1, (d) Hf-DZ-1, (e) Ti-DZ-1, (f) Zr-DZ-1, (g) DZ-1, and (h) ERB-1-del-135 recorded after pyridine adsorption at  $25 \text{ }^\circ\text{C}$  and desorption at  $150 \text{ }^\circ\text{C}$ .

$1542 \text{ cm}^{-1}$  correspond to pyridine bound to Brønsted acid sites ( $\text{PyH}^+$ ) and Lewis acid sites ( $\text{PyL}$ ), respectively, and are clearly observed for ERB-1-del-135, as shown in Figure 5h. As expected, the  $1542 \text{ cm}^{-1}$   $\text{PyH}^+$  band for DZ-1 and all investigated heteroatom-substituted DZ-1 materials is weak, and its residual intensity at  $1542 \text{ cm}^{-1}$  is most likely due to the small amount of B ( $\text{Si}/\text{B} = 73$ ) residing in the framework following delamination and heteroatom reinsertion. A weak band at  $1457 \text{ cm}^{-1}$  is observed for both DZ-1 and Ti-DZ-1 in Figures 5g,e. This is assigned to residual framework B, because such a band has been previously ascribed to Lewis acid sites formed by framework B sites in zeolite B-Beta.<sup>26</sup> Ti-DZ-1 also contains a band at  $1444 \text{ cm}^{-1}$ , which has been previously assigned to framework Ti Lewis acid sites in TS-1.<sup>27</sup> Although DZ-1 materials consisting of other substituted heteroatoms show very weak bands associated with adsorbed pyridine, Sn-DZ-1 shows a prominent band at  $1451 \text{ cm}^{-1}$ , which is assigned to Lewis acid sites. The infrared band at  $1490 \text{ cm}^{-1}$  corresponds to the superposition of signals of both

Brønsted and Lewis adsorbed  $\text{PyH}^+$  and  $\text{PyL}$  species, respectively.

#### Solid-State Diffuse Reflectance Ultraviolet (DR-UV) Spectroscopy.

For metal heteroatoms located in a silicate framework, there are distinct charge transfer transitions involving framework oxygen anions and framework metal cations, which are typically located in the UV region.<sup>28,29</sup> These transitions have a higher energy upon lowering the degree of aggregation of the heteroatom metal oxide, up to the extreme of an isolated grafted metal cation on a support. We performed DR-UV spectroscopy to investigate the degree of isolation of the heteroatoms (i.e., Sn, Ti, Zr, Hf, Nb, and Ta) within heteroatom-substituted DZ-1, and data are shown in Figure 6a–f. The DR-UV spectrum of Sn-DZ-1 shows a very narrow and sharp band centered at  $200 \text{ nm}$ , which suggests that the Sn sites in this material are isolated within a tetrahedral coordination environment.<sup>30</sup>

The DR-UV spectrum of Ti-DZ-1 consists of bands within the range of  $210\text{--}230 \text{ nm}$ . These bands have been previously assigned to isolated Ti sites in the TS-1 framework as well as in MCM-41, which have a coordination number of either four or six (attributed to water coordination).<sup>31,32</sup> Zr-DZ-1 (Figure 6c) and Ta-DZ-1 (Figure 6f) show absorption bands centered at  $220$  and  $219 \text{ nm}$ , respectively, in their DR-UV spectra, which indicates the successful incorporation of these heteroatoms within a tetrahedral coordination environment in DZ-1. The DR-UV spectra of Hf-DZ-1 (Figure 6d) and Nb-DZ-1 (Figure 6e) also consist of absorption bands, both centered at  $237 \text{ nm}$ , that are more similar to that of Ti-DZ-1, suggesting a similar degree of site isolation in these materials.

#### Baeyer–Villiger Oxidation over Heteroatom-Substituted Lewis Acid Zeolite Catalysts.

We confirmed the catalytic accessibility and activity of heteroatoms substituted in delaminated Lewis acid zeolites using the Baeyer–Villiger oxidation of 2-adamantanone with aqueous hydrogen peroxide at  $75 \text{ }^\circ\text{C}$  as a probe reaction, the chemical equation of which is shown in Scheme 1a. We compared the catalytic performance of DZ-1-based delaminated zeolites consisting of different metal heteroatomss; the kinetics data are shown in Figure 7 and are summarized in Table 2. The kinetic data in Figure 7 show a linear relationship between the conversion of 2-adamantanone and time, consisting of the previously observed zeroth order dependence on 2-adamantanone. As expected, metal-free catalyst consisting of all-silica DZ-1 shows negligible activity for the oxidation of 2-adamantanone. Sn-DZ-1 shows significantly higher activity than other heteroatom-substituted DZ-1 materials consisting of either Ti, Zr, Hf, Nb, or Ta heteroatoms. Note, however, that all DZ-1-based catalysts show nearly 100% product selectivity.

Next, to investigate the reactivity and accessibility of Sn sites that are located in two vastly differing zeolitic environments (i.e., microporous versus delaminated), we compared the catalytic activity of Sn-DZ-1 ( $\text{Si}/\text{Sn} = 65$ ) and Sn-Beta ( $\text{Si}/\text{Sn} = 100$ ) for Baeyer–Villiger oxidation using ketones of varying steric bulk, as shown in Scheme 1b and c. Sn-Beta has been previously reported to be an active and selective catalyst for Baeyer–Villiger oxidation,<sup>11</sup> in which the Sn sites are located within the 3D 12-MR pores and BEA channel system at certain specific, uniform crystallographic positions.<sup>33</sup> This is entirely in contrast to Sn-DZ-1, in which the Sn sites are expected to be located within 12-MR pockets that are near the external surface. Therefore, the accessibility of the Sn sites in two materials is hypothesized to be vastly different and can be examined using bulky substrates. Baeyer–Villiger kinetics data in Figure 8a and Table 3 show that

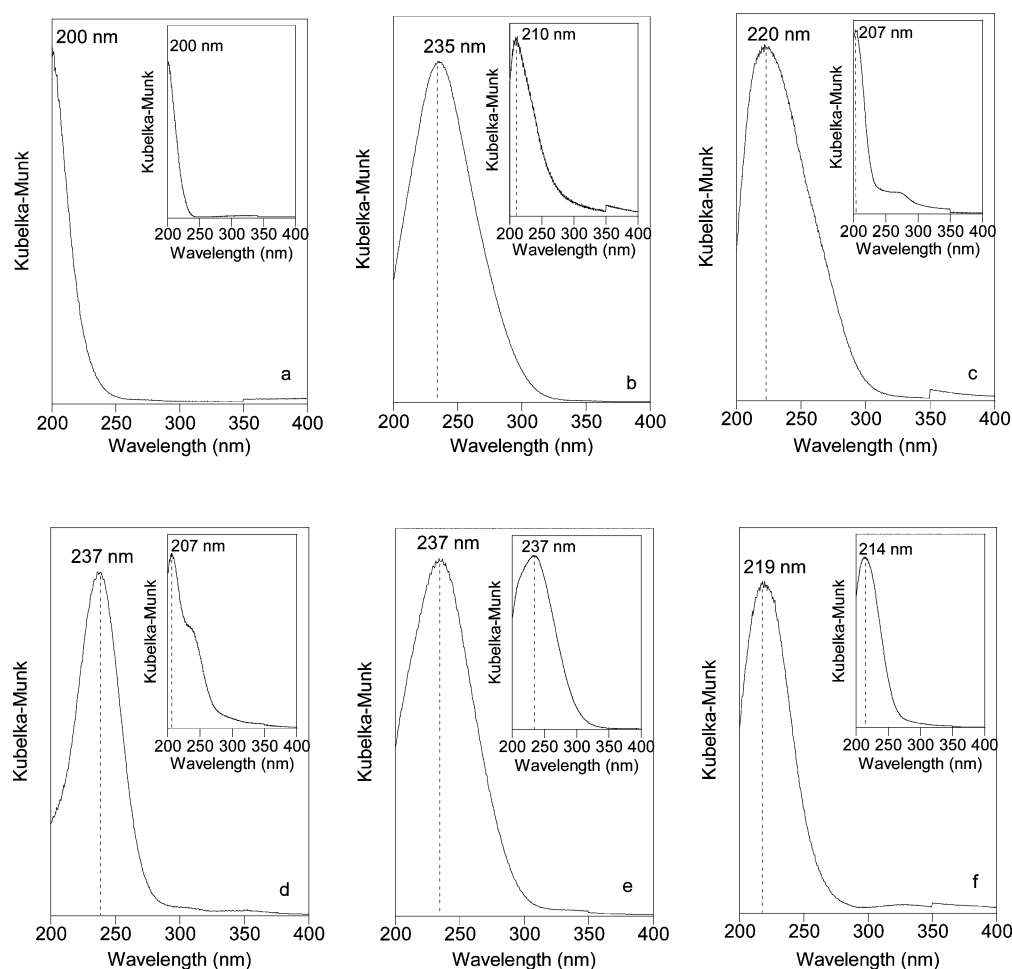
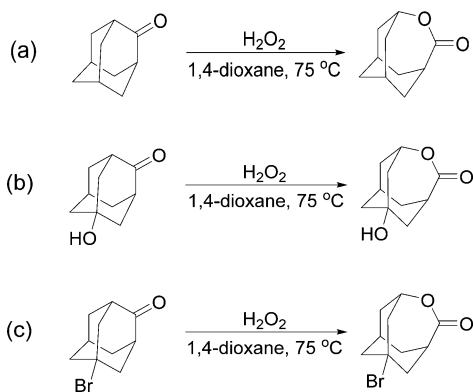


**Figure 6.** DR-UV data characterizing (a) Sn-DZ-1, (b) Ti-DZ-1, (c) Zr-DZ-1, (d) Hf-DZ-1, (e) Nb-DZ-1, and (f) Ta-DZ-1. The inset shows the DR-UV data characterizing the samples after acid treatment.

**Scheme 1. Chemical Equations of Baeyer–Villiger oxidation of 2-Adamantanone Derivatives with  $H_2O_2$**



when 2-adamantanone is used as the ketone substrate, Sn-Beta shows significantly higher activity than Sn-DZ-1 ( $1963 \text{ mol h}^{-1} (\text{mol Sn})^{-1}$  for Sn-Beta vs  $866 \text{ mol h}^{-1} (\text{mol Sn})^{-1}$  for Sn-DZ-1). However, as shown in Figure 8b, when using the sterically more demanding 5-hydroxyl-2-adamantanone as the ketone substrate, Sn-DZ-1 shows significantly higher activity than Sn-Beta ( $825 \text{ mol h}^{-1} (\text{mol Sn})^{-1}$  for Sn-DZ-1 vs  $417 \text{ mol h}^{-1} (\text{mol Sn})^{-1}$  for Sn-Beta), which suggests that the activity for Sn-Beta is now limited by the more restricted accessibility of this reactant, compared with the delaminated Sn-DZ-1, in which all Sn sites are

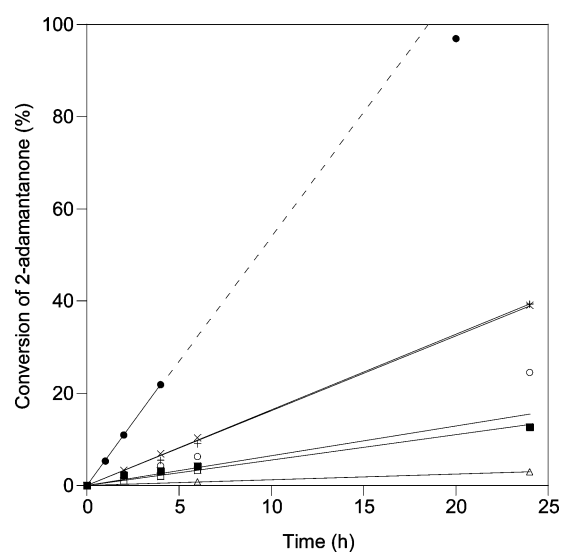


**Figure 7.** Catalysis kinetics of 2-adamantanone reacting with  $H_2O_2$  over DZ-1 related materials: DZ-1 ( $\Delta$ ), Sn-DZ-1 (Si/Sn = 65) ( $\bullet$ ), Ti-DZ-1 (Si/Ti = 67) ( $\circ$ ), Zr-DZ-1 (Si/Zr = 57) ( $\blacksquare$ ), Hf-DZ-1 (Si/Hf = 62) ( $\square$ ), Nb-DZ-1 (Si/Nb = 40) ( $\times$ ), and Ta-DZ-1 (Si/Ta = 39) ( $+$ ). Reaction conditions: 30 wt %  $H_2O_2$  in  $H_2O$ ;  $H_2O_2$ /2-adamantanone = 1.5:1 by mol; 1,4-dioxane as solvent; 75 °C. Molar ratio of Sn to ketone = 0.0066:1.

**Table 2. BV Oxidation of 2-Adamantanone with H<sub>2</sub>O<sub>2</sub> Catalyzed by DZ-1 Related Materials<sup>a</sup>**

substrates	initial rates <sup>b</sup> [mol h <sup>-1</sup> (mol Sn) <sup>-1</sup> ]	C <sup>c</sup> (%)
DZ-1	26	3
Sn-DZ-1	866	97
Ti-DZ-1	161	18
Zr-DZ-1	114	13
Hf-DZ-1	260	29
Nb-DZ-1	81	9
Ta-DZ-1	221	25

<sup>a</sup>Reaction condition: 30 wt % H<sub>2</sub>O<sub>2</sub> in H<sub>2</sub>O; H<sub>2</sub>O<sub>2</sub>/2-adamantanone = 1.5:1 by mol; 1,4-dioxane as solvent; 75 °C. Molar ratio of Sn to ketone = 0.0066:1. <sup>b</sup>Initial rates are calculated by dividing the moles of substrates converted per hour when conversion of substrate is under 20% by moles of Sn sites. <sup>c</sup>Conversion = (moles of ketone converted at 24 h)/(initial moles of ketone) × 100. Selectivities for all these catalysts are nearly 100%.

located near the external surface. Similarly, as shown in Figure 8c, when 5-bromo-2-adamantanone is used as the ketone substrate, Sn-DZ-1 exhibits noticeably better performance than Sn-Beta (688 mol h<sup>-1</sup> (mol Sn)<sup>-1</sup> for Sn-DZ-1 vs 366 mol h<sup>-1</sup> (mol Sn)<sup>-1</sup> for Sn-Beta). As summarized in Table 3, when the size of the ketone substrate increases from 2-adamantanone to 5-bromo-2-adamantanone, the catalytic activity of Sn-DZ-1 for Baeyer–Villiger oxidation has only decreased by 20%, but the same activity for Sn-Beta catalyst has decreased by 81%. Therefore, it is evident that the Sn sites in Sn-DZ-1 prepared according to our heteroatom-substitution method yields higher accessibility than Sn sites located in internal micropores of three-dimensional zeolites.

To investigate the relationship between the catalytic activity for Baeyer–Villiger oxidation and the proximity of the Sn sites, we synthesized two batches of Sn-DZ-1 with different Sn contents, which were accomplished by varying the synthesis time. These two Sn-DZ-1 samples have Si/Sn ratios of 65 and 94. If the reaction requires two Sn sites to work cooperatively, we should expect that the one with lower Si/Sn ratios should have disproportionately higher catalytic activity than the one with higher Si/Sn ratios. The catalytic results shown in Figure 9 and summarized in Table 4 suggest that the per-Sn-site activity for each sample is similar: 866 mol h<sup>-1</sup> (mol Sn)<sup>-1</sup> for Sn-DZ-1 with Si/Sn = 65 and 767 mol h<sup>-1</sup> (mol Sn)<sup>-1</sup> for Sn-DZ-1 with Si/Sn = 94. Therefore, these results suggest that activity for Baeyer–Villiger oxidation is independent of the local density of Sn sites and may likely be accomplished with an isolated Sn site. Such a conclusion is consistent with previously proposed mechanisms.<sup>11</sup>

We also wanted to compare two delaminated zeolite environments for Sn sites, consisting of Sn-DZ-1 (Si/Sn = 65) and Sn-UCB-4 (Si/Sn = 100), for the Baeyer–Villiger oxidation of 2-adamantanone. Relevant kinetics data are shown in Figure 10 and summarized in Table 5, and demonstrate that Sn-DZ-1 is significantly more active than Sn-UCB-4 (866 mol h<sup>-1</sup> (mol Sn)<sup>-1</sup> for Sn-DZ-1 vs 355 mol h<sup>-1</sup> (mol Sn)<sup>-1</sup> for Sn-UCB-4), even though they have very similar external surface areas and DR-UV spectra of isolated framework Sn sites. These results suggest that the zeolite framework type has a significant impact on the reactivity for Lewis acid-catalyzed reactions. The latter is known when dealing with Ti heteroatom sites in three-dimensional zeolites and hydrogen peroxide as oxidant, in which Ti-beta showed a different selectivity and activity compared with TS-1 (Ti in silicalite MFI structure).<sup>9</sup> The results shown here suggest

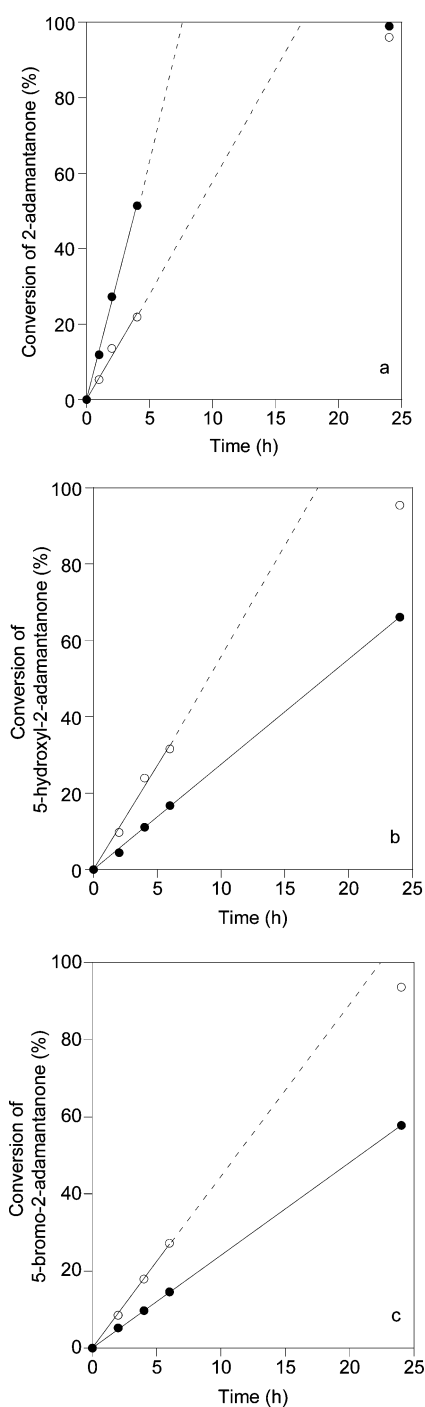


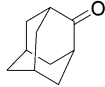
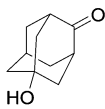
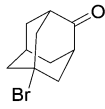
**Figure 8.** Catalysis kinetics of (a) 2-adamantanone, (b) 5-hydroxyl-2-adamantanone, and (c) 5-bromo-2-adamantanone reacting with H<sub>2</sub>O<sub>2</sub> over Sn-DZ-1 (Si/Sn = 65) (○) and Sn-Beta (Si/Sn = 100) (●). Reaction conditions: 30 wt % H<sub>2</sub>O<sub>2</sub> in H<sub>2</sub>O; H<sub>2</sub>O<sub>2</sub>/ketone = 1.5:1 by mol; 1,4-dioxane as solvent; 75 °C. Molar ratio of Sn to ketone = 0.0066:1.

the framework to make a catalytic difference even for half-open sites such as those found near the external surface of delaminated zeolites.

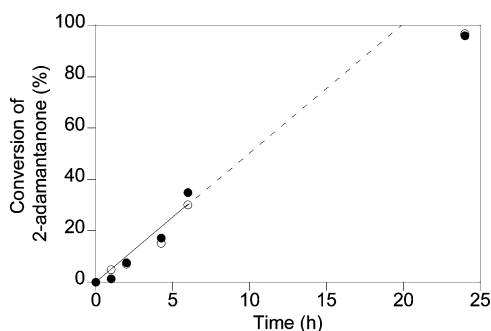
In addition to steric the constraints discussed above, the half-open sites in Sn-DZ-1 interact completely differently with a fluid-phase solvent relative to those immersed within the internal porosity of Sn-Beta. Although the latter are known to be active for glucose isomerization,<sup>13,15</sup> in which hydrophobicity of the



**Table 3. BV Oxidation of 2-Adamantanone Derivatives with H<sub>2</sub>O<sub>2</sub> Catalyzed by Sn-DZ-1 and Sn-Beta<sup>a</sup>**

Substrates	Sn-DZ-1 <sup>b</sup>		Sn-Beta <sup>c</sup>	
	Initial rates <sup>d</sup>	C <sup>e</sup>	Initial rates <sup>d</sup>	C <sup>e</sup>
	[mol h <sup>-1</sup> (mol Sn) <sup>-1</sup> ]	(%)	[mol h <sup>-1</sup> (mol Sn) <sup>-1</sup> ]	(%)
	866	97	1963	99
	825	95	417	66
	688	94	366	57

<sup>a</sup>Reaction conditions: 30 wt % H<sub>2</sub>O<sub>2</sub> in H<sub>2</sub>O; H<sub>2</sub>O<sub>2</sub>/ketone = 1.5:1 by mol; 1,4-dioxane as solvent; 75 °C. Molar ratio of Sn to ketone = 0.0066:1. <sup>b</sup>Si/Sn = 65. <sup>c</sup>Si/Sn = 100. <sup>d</sup>Initial rates are calculated by dividing the moles of substrates converted per hour when conversion of substrate is under 20% by moles of Sn sites. <sup>e</sup>Conversion = (moles of ketone converted at 24 h)/(initial moles of ketone) × 100. <sup>f</sup>Selectivity = (moles of product at 24 h)/(moles of ketone reacted) × 100. Selectivities for all these catalysts are nearly 100%.

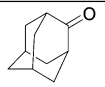


**Figure 9.** Catalysis kinetics of 2-adamantanone reacting with H<sub>2</sub>O<sub>2</sub> over Sn-DZ-1 materials that have Si/Sn ratios of 65 (○) and 94 (●). Reaction conditions: 30 wt % H<sub>2</sub>O<sub>2</sub> in H<sub>2</sub>O; H<sub>2</sub>O<sub>2</sub>/2-adamantanone = 1.5:1 by mol; 1,4-dioxane as solvent; 75 °C. Molar ratio of Sn to ketone = 0.0066:1.

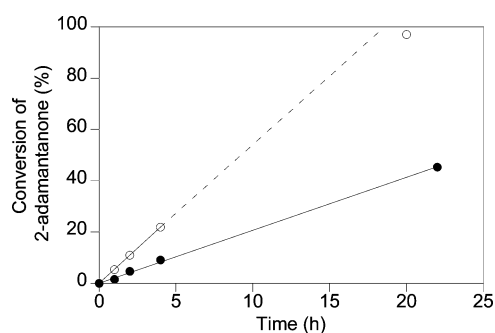
zeolite framework is invoked to be crucial for catalysis, the open environment of Lewis acid sites in Sn-DZ-1 results in a lack of selective glucose-to-fructose isomerization activity.

**Olefin Epoxidation Using Organic Hydroperoxide.** We investigated the accessibility and catalytic activity of Ti-substituted Lewis acid zeolite catalysts, using olefin epoxidation with *tert*-butyl-hydroperoxide (TBHP) as oxidant, as shown in Scheme 2. Although we use this as a relevant probe reaction for investigating Ti heteroatom sites, it is also industrially relevant in the synthesis of propylene oxide from propylene, in which organic hydroperoxides are used as oxidant.<sup>34</sup> Catalysis data for 1-octene at 60 °C are shown in Figure 11 and are also summarized in Table 6. The Ti-UCB-4 catalyst has an initial rate of catalysis normalized per Ti atom that is 5-fold faster than both Ti-DZ-1 and Ti/SiO<sub>2</sub> catalysts. Even at a low TBHP conversion of 20–30%, the selectivity (defined as epoxide formed divided by TBHP consumed) is above 90% for all delaminated-zeolite-based

**Table 4. BV Oxidation of 2-Adamantanone with H<sub>2</sub>O<sub>2</sub> Catalyzed by Sn-DZ-1 with Different Sn Content<sup>a</sup>**

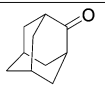
Substrates	Sn-DZ-1 (Si/Sn = 65)		Sn-DZ-1 (Si/Sn = 94)	
	Initial rates <sup>b</sup>	C <sup>c</sup>	Initial rates <sup>b</sup>	C <sup>c</sup>
	[mol h <sup>-1</sup> (mol Sn) <sup>-1</sup> ]	(%)	[mol h <sup>-1</sup> (mol Sn) <sup>-1</sup> ]	(%)
	866	97	767	86

<sup>a</sup>Reaction conditions: 30 wt % H<sub>2</sub>O<sub>2</sub> in H<sub>2</sub>O; H<sub>2</sub>O<sub>2</sub>/2-adamantanone = 1.5:1 by mol; 1,4-dioxane as solvent; 75 °C. Molar ratio of Sn to ketone = 0.0066:1. <sup>b</sup>Initial rates are calculated by dividing the moles of substrates converted per hour when conversion of substrate is under 20% by moles of Sn sites. <sup>c</sup>Conversion = (moles of ketone converted at 24 h)/(initial moles of ketone) × 100. <sup>d</sup>Selectivity = (moles of product at 24 h)/(moles of ketone reacted) × 100.



**Figure 10.** Catalysis kinetics of 2-adamantanone reacting with H<sub>2</sub>O<sub>2</sub> over Sn-DZ-1 (Si/Sn = 65) (○) and Sn-UCB-4 (Si/Sn = 100) (●) materials that have Si/Sn ratios of 65 and 100, respectively. Reaction conditions: 30 wt % H<sub>2</sub>O<sub>2</sub> in H<sub>2</sub>O; H<sub>2</sub>O<sub>2</sub>/2-adamantanone = 1.5:1 by mol; 1,4-dioxane as solvent; 75 °C. Molar ratio of Sn to ketone = 0.0066:1.

**Table 5. BV Oxidation of 2-Adamantanone with H<sub>2</sub>O<sub>2</sub> Catalyzed by Sn-DZ-1 with Different Sn Content<sup>a</sup>**

Substrates	Sn-DZ-1 (Si/Sn = 65)		Sn-UCB-4 (Si/Sn = 100)	
	Initial rates <sup>b</sup>	C <sup>c</sup>	Initial rates <sup>b</sup>	C <sup>c</sup>
	[mol h <sup>-1</sup> (mol Sn) <sup>-1</sup> ]	(%)	[mol h <sup>-1</sup> (mol Sn) <sup>-1</sup> ]	(%)
	866	97	355	45

<sup>a</sup>Reaction conditions: 30 wt % H<sub>2</sub>O<sub>2</sub> in H<sub>2</sub>O; H<sub>2</sub>O<sub>2</sub>/2-adamantanone = 1.5:1 by mol; 1,4-dioxane as solvent; 75 °C. Molar ratio of Sn to ketone = 0.0066:1. <sup>b</sup>Initial rates are calculated by dividing the moles of substrates converted per hour when conversion of substrate is under 20% by moles of Sn sites. <sup>c</sup>Conversion = (moles of ketone converted at 24 h)/(initial moles of ketone) × 100. <sup>d</sup>Selectivity = (moles of product at 24 h)/(moles of ketone reacted) × 100.

catalysts, which is much higher than typical selectivities for an amorphous Ti/SiO<sub>2</sub> catalyst at the same conversion for the same reaction, as shown in Table 6. The higher activity of Ti-UCB-4 is also apparent considering the number of turnovers (TON) at 2 h of reaction time, which is 3.6- and 4.5-fold higher for Ti-UCB-4 relative to Ti-DZ-1 and Ti/SiO<sub>2</sub>, respectively.

Epoxidation of 1-octene was also performed under more forcing conditions, corresponding to a higher TBHP concen-

## Scheme 2. Chemical Equation of Epoxidation of Olefins with TBHP

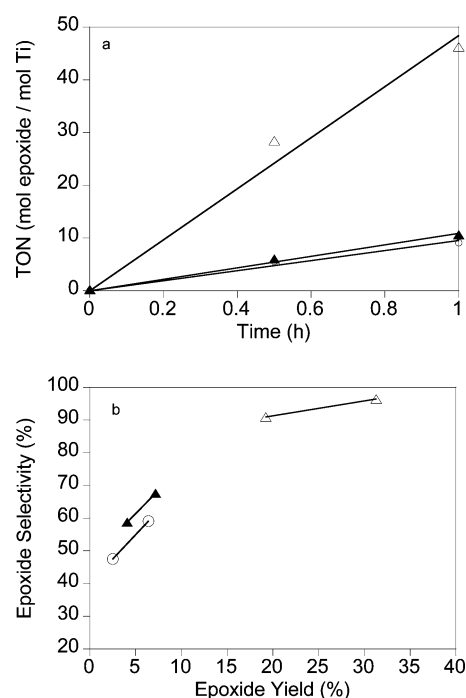
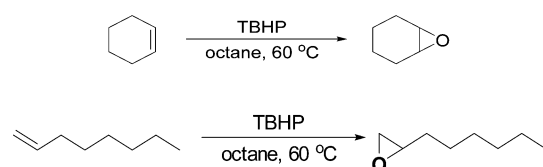


**Figure 11.** (a) Catalytic kinetics of time versus TON normalized by mmol Ti sites and (b) epoxide yield versus epoxide selectivity of 1-octene reacting with TBHP over Ti-UCB-4 ( $\Delta$ ), Ti-DZ-1 ( $\blacktriangle$ ), and Ti/SiO<sub>2</sub> (O) materials.

tration and at a higher temperature (110 °C). Results are represented in Figure 12 and summarized in Table 6. Under these conditions, Ti-UCB-4 is both the most active and the most selective among the delaminated-zeolite catalysts tested here, having an initial rate per Ti site that is 3.2-fold higher than Ti-DZ-1. This again demonstrates how the choice of zeolite framework

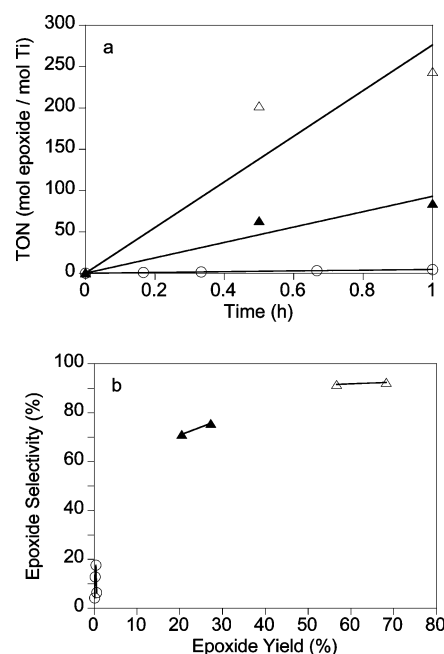


**Figure 12.** (a) Catalytic kinetics of time versus TON normalized by mmol Ti sites and (b) epoxide yield versus epoxide selectivity of 1-octene reacting with TBHP over Ti-UCB-4 ( $\Delta$ ), Ti-DZ-1 ( $\blacktriangle$ ), and Ti/SiO<sub>2</sub> (O) materials.

(MWW type of framework in DZ-1 versus SSZ-70 in UCB-4) controls the Ti catalyst epoxidation activity and selectivity. Under the same conditions, Ti/SiO<sub>2</sub> shows poor activity and selectivity relative to both zeolite catalysts Ti-DZ-1 and Ti-UCB-4, as shown in Figure 12 and Table 6. This reinforces the benefit of having Ti within a zeolitic rather than amorphous framework, and this benefit is further made clear by a comparison of the initial rate differences per Ti site for the zeolitic Ti-UCB-4 and amorphous silica Ti catalysts, which differ by more than 17-fold.

We also investigated whether the general superiority and robustness of the delaminated zeolite-based catalysts also holds for the epoxidation of internal olefins. Cyclohexene was also tested for epoxidation by TBHP over these catalysts. Results are represented in Figure 13 and summarized in Table 6. From the kinetics data, it is evident that the epoxidation kinetics are not first-order for both zeolite catalysts, since the rates do not deviate

**Table 6.** Epoxidation of Olefins with TBHP Catalyzed by Various Zeolite Catalysts

sample	Ti (wt %)	reactant	reaction condition <sup>a</sup> (T °C)	k <sup>b</sup> (mol epoxide/mol Ti × ks)	TON <sup>c</sup>	TBHP efficiency (%) <sup>d</sup>	epoxide selectivity (%)
Ti-DZ-1	0.98	cyclohexene	A (60)	32	86	99	>99
		1-octene	B (60)	3	20	24	70
		1-octene	C (110)	35	100	36	63
Ti-UCB-4	0.76	cyclohexene	A (60)	80	128	99	>99
		1-octene	B (60)	15	72	72	97
		1-octene	C (110)	112	262	76	84
Ti/SiO <sub>2</sub>	0.77	cyclohexene	A (60)	39	88	72	76
		1-octene	B (60)	3	16	22	77
		1-octene	C (110)	2	9	3	26
TS-1	0.85	cyclohexene	A (60)	0	0	0	n/a

<sup>a</sup>Reaction conditions: (A) 25 mg of zeolite catalyst, 0.59 mmol of TBHP, 5.9 mmol of cyclohexene, 20 mL of octane as solvent, 60 °C; (B) 25 mg of zeolite catalyst, 0.59 mmol of TBHP, 5.9 mmol of 1-octene, 20 mL of octane as solvent, 60 °C; (C) 25 mg of catalyst, 1.5 mmol of TBHP, 3.0 mmol of 1-octene, 10 mL of octane as solvent, 110 °C; (D) 25 mg of catalyst, 1.2 mmol of TBHP, 4.8 mmol of cyclohexene, 3 mL of chloroform as solvent, 60 °C. <sup>b</sup>k is calculated when the epoxide yield is under 20%. <sup>c</sup>TON values are calculated by dividing the moles of epoxide formed at 2 h by the moles of Ti sites. <sup>d</sup>TBHP efficiency is calculated by dividing the moles of epoxide formed at 5 h by the moles of TBHP at 0 h.

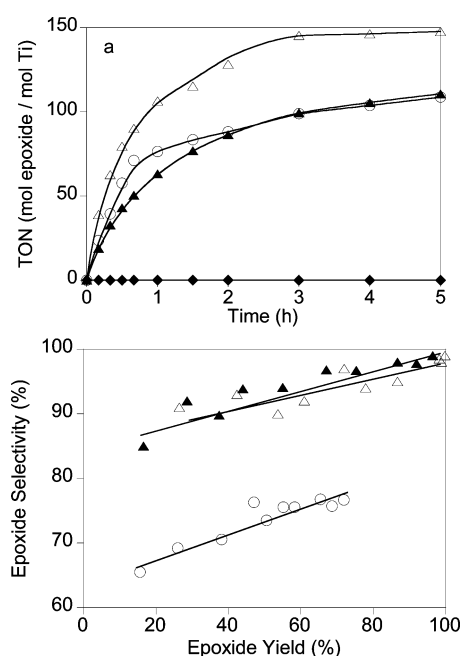


**Figure 13.** (a) Catalytic kinetics of time versus TON normalized by mmol Ti sites and (b) epoxide yield versus epoxide selectivity of cyclohexene reacting with TBHP over Ti-UCB-4 ( $\Delta$ ), Ti-DZ-1 ( $\blacktriangle$ ), Ti/SiO<sub>2</sub> ( $\circ$ ), and TS-1 ( $\blacklozenge$ ) materials. Reaction conditions: 25 mg of catalyst, 0.59 mmol of TBHP, 5.9 mmol of cyclohexene, 20 mL of octane as solvent, 60 °C.

significantly from the initial rate, even at a conversion of  $\sim$ 70% for both Ti-UCB-4 and Ti-DZ-1. On the other hand, above 50% conversion, the amorphous Ti/SiO<sub>2</sub> catalyst severely deactivates under the same conditions. Both Ti delaminated-zeolite catalysts also exhibit higher epoxide selectivity than Ti/SiO<sub>2</sub>, as observed above for the terminal olefin epoxidation. Thus, both the activity and selectivity of the Ti-zeolite catalysts are superior to the amorphous silica catalyst.

## CONCLUSIONS

Heteroatom metal cations consisting of Hf, Nb, Ti, Ta, Sn, and Zr are reinserted into silanol nests within DZ-1, and a subset of these are also reinserted into deboronated UCB-4 as a comparison, all by using reactive metal precursors. In all DZ-1-based systems, metal heteroatom reinsertion is accompanied by synthesis of a greater degree of delamination according to N<sub>2</sub> physisorption data. Diffuse reflectance UV spectroscopy and elemental analysis confirm the existence of isolated framework heteroatoms upon reinsertion. Pyridine adsorption of heteroatom-substituted DZ-1 investigated by IR spectroscopy shows that the heteroatom metal sites have Lewis acid characteristics, and this is particularly so for Sn-DZ-1, which has a strong adsorption band at 1457 cm<sup>-1</sup> that suggests strong Lewis acidity. Of all heteroatoms investigated, Sn-DZ-1 is the most active among DZ-1-based materials tested for Baeyer–Villiger oxidation. When the small reactant 2-adamantone is used as the ketone substrate, a reference material Sn-Beta shows higher activity than Sn-DZ-1, but when bulkier ketone substrates (such as 5-hydroxyl-2-adamantone and 5-bromo-2-adamantone) are used as the ketone substrates, Sn-DZ-1 shows a significantly higher activity than Sn-Beta, probably because of the higher accessibility of the Sn sites located in Sn-DZ-1 than in Sn-Beta. When we vary the concentration of framework Sn incorporated

in DZ-1, the activity for Baeyer–Villiger oxidation of 2-adamantone per site is the same, and this suggests that the Baeyer–Villiger oxidation requires isolated Sn sites. The role of the framework is first highlighted in catalysis with a comparison of Sn-DZ-1 and Sn-UCB-4 as Baeyer–Villiger oxidation catalysts, in which Sn-UCB-4 is much less active than Sn-DZ-1, even though the external surface areas and DR-UV spectra for both materials of the two delaminated zeolite materials are similar. Among the heteroatom-substituted delaminated zeolites, only Ti-substituted delaminated zeolites (Ti-DZ-1 and Ti-UCB-4 in this study) are active for cyclohexene epoxidation with TBHP. Interestingly, Ti-UCB-4 is about 1.6-fold more active than Ti-DZ-1, which is another example that the zeolite framework type plays an important role in Lewis acid-catalyzed reactions, even when sites are located near the external surface, and further differentiates these systems with their amorphous Ti/SiO<sub>2</sub> counterpart, for which the delaminated zeolites are observed to be up to 17-fold more active per Ti site.

## ASSOCIATED CONTENT

### Supporting Information

The following file is available free of charge on the ACS Publications website at DOI: 10.1021/cs5020546.

Description of characterization methods for PXRD and solid-state NMR spectroscopy, figures of PXRD patterns, figures of <sup>29</sup>Si MAS and <sup>29</sup>Si CPMAS NMR spectroscopy data, TEM images, figures of DR-UV spectroscopy data, and table of unit-cell parameters ([PDF](#))

## AUTHOR INFORMATION

### Corresponding Authors

\*E-mail: sizo@chevron.com.

\*E-mail: askatz@berkeley.edu.

### Notes

The authors declare no competing financial interest.

## ACKNOWLEDGMENTS

The authors are grateful to the Management and Transfer of Hydrogen via Catalysis Program funded by Chevron Corporation. The NMR facility at Caltech was supported by the National Science Foundation under Grant No. 9724240 and supported in part by the MRSEC Program of the NSF under Award No. DMR-520565. X.O. is also grateful to Marat Orazov, Josh Pacheco, and Prof. Mark E. Davis at Caltech for providing Sn-Beta, TS-1, and other materials, as well as catalytic testing of materials for glucose-to-fructose isomerization.

## REFERENCES

- (1) Notari, B. *Adv. Catal.*; Eley, D. D., Haag, W. O., Gates, B., Eds.; Academic Press: New York, 1996, Vol. 41, p 253–334.
- (2) Blasco, T.; Cambor, M. A.; Corma, A.; Perez-Pariente, J. *J. Am. Chem. Soc.* **1993**, *115*, 11806–11813.
- (3) Blasco, T.; Corma, A.; Navarro, M. T.; Pariente, J. P. *J. Catal.* **1995**, *156*, 65–74.
- (4) Taramasso, M.; Perego, G.; Notari, B. U.S. Patent 4,410,501, 1983.
- (5) Taramasso, M.; Manara, G.; Fattore, V.; Notari, B. U.S. Patent 4,666,692, 1987.
- (6) Bellussi, G.; Buonomo, F.; Esposito, A.; Clerici, M. G.; Romano, U.; Notari, B. U.S. Patent 4,701,428, 1987.
- (7) Cambor, M. A.; Corma, A.; Perezpariente, J. *Zeolites* **1993**, *13*, 82–87.
- (8) Serrano, D. P.; Li, H.-X.; Davis, M. E. *J. Chem. Soc., Chem. Commun.* **1992**, 745–747.

- (9) Dartt, C. B.; Davis, M. E. *Appl. Catal., A* **1996**, *143*, 53–73.
- (10) Wu, P.; Tatsumi, T. *Chem. Commun.* **2002**, 1026–1027.
- (11) Corma, A.; Nemeth, L. T.; Renz, M.; Valencia, S. *Nature* **2001**, *412*, 423–425.
- (12) Renz, M.; Blasco, T.; Corma, A.; Fornes, V.; Jensen, R.; Nemeth, L. *Chem. - Eur. J.* **2002**, *8*, 4708–4717.
- (13) Moliner, M.; Roman-Leshkov, Y.; Davis, M. E. *Proc. Natl. Acad. Sci. U. S. A.* **2010**, *107*, 6164–6168.
- (14) Bermejo-Deval, R.; Assary, R. S.; Nikolla, E.; Moliner, M.; Roman-Leshkov, Y.; Hwang, S.-J.; Palsdottir, A.; Silverman, D.; Lobo, R. F.; Curtiss, L. A.; Davis, M. E. *Proc. Natl. Acad. Sci. U. S. A.* **2012**, *109*, 9727–9732.
- (15) Bermejo-Deval, R.; Gounder, R.; Davis, M. E. *ACS Catal.* **2012**, *2*, 2705–2713.
- (16) Pacheco, J. J.; Davis, M. E. *Proc. Natl. Acad. Sci. U. S. A.* **2014**, *111*, 8363–8367.
- (17) Ouyang, X.; Wanglee, Y.-J.; Hwang, S.-J.; Xie, D.; Rea, T.; Zones, S. I.; Katz, A. *Dalton Trans.* **2014**, *43*, 10417–10429.
- (18) Ogino, I.; Eilertsen, E. A.; Hwang, S.-J.; Rea, T.; Xie, D.; Ouyang, X.; Zones, S. I.; Katz, A. *Chem. Mater.* **2013**, *25*, 1502–1509.
- (19) Artioli, G.; Lamberti, C.; Marra, G. L. *Acta Crystallogr., Sect. B: Struct. Sci.* **2000**, *56*, 2–10.
- (20) Bordiga, S.; Roggero, L.; Ugliengo, P.; Zecchina, A.; Bolis, V.; Artioli, G.; Buzzoni, R.; Marra, G.; Rivetti, F.; Spano, G.; Lamberti, C. *Dalton Trans.* **2000**, 3921–3929.
- (21) Ouyang, X.; Hwang, S.-J.; Runnebaum, R. C.; Xie, D.; Wanglee, Y.-J.; Rea, T.; Zones, S. I.; Katz, A. *J. Am. Chem. Soc.* **2013**, *136*, 1449–1461.
- (22) Archer, R. H.; Carpenter, J. R.; Hwang, S.-J.; Burton, A. W.; Chen, C.-Y.; Zones, S. I.; Davis, M. E. *Chem. Mater.* **2010**, *22*, 2563–2572.
- (23) Archer, R. H.; Zones, S. I.; Davis, M. E. *Microporous Mesoporous Mater.* **2010**, *130*, 255–265.
- (24) Wu, P.; Nuntasri, D.; Ruan, J.; Liu, Y.; He, M.; Fan, W.; Terasaki, O.; Tatsumi, T. *J. Phys. Chem. B* **2004**, *108*, 19126–19131.
- (25) Ravikovitch, P. I.; Haller, G. L.; Neimark, A. V. *Adv. Colloid Interface Sci.* **1998**, *76*, 203–226.
- (26) Corma, A.; Domine, M. E.; Valencia, S. *J. Catal.* **2003**, *215*, 294–304.
- (27) Bonino, F.; Damin, A.; Bordiga, S.; Lamberti, C.; Zecchina, A. *Langmuir* **2003**, *19*, 2155–2161.
- (28) Boccuti, M. R.; Rao, K. M.; Zecchina, A.; Leofanti, G.; Petrini, G. In *Structure and Reactivity of Surfaces*; Morterra, C., Zecchina, A., Costa, G., Eds.; Elsevier: Amsterdam, 1989; p 133–144.
- (29) Zecchina, A.; Spoto, G.; Bordiga, S.; A. F.; Petrini, G.; Leofanti, G.; Padovan, M., In *Zeolite Chemistry and Catalysis*; Jacobs, P. A., Jaeger, N. I., Kubelková, L., Wichterlová, B., Eds.; Elsevier: Amsterdam, 1991; p 251–258.
- (30) Luo, H. Y.; Bui, L.; Gunther, W. R.; Min, E.; Román-Leshkov, Y. *ACS Catal.* **2012**, *2*, 2695–2699.
- (31) Geobaldo, F.; Bordiga, S.; Zecchina, A.; Giamello, E.; Leofanti, G.; Petrini, G. *Catal. Lett.* **1992**, *16*, 109–115.
- (32) Corma, A.; Navarro, M. T.; Pariente, J. P. *J. Chem. Soc., Chem. Commun.* **1994**, 147–148.
- (33) Bare, S. R.; Kelly, S. D.; Sinkler, W.; Low, J. J.; Modica, F. S.; Valencia, S.; Corma, A.; Nemeth, L. T. *J. Am. Chem. Soc.* **2005**, *127*, 12924–12932.
- (34) Buijink, J. K. F.; Lange, J.-P.; Bos, A. N. R.; Horton, A. D.; Niele, F. G. M. In *Mechanisms in Homogeneous and Heterogeneous Epoxidation Catalysis*; Oyama, S. T., Ed.; Elsevier: Amsterdam, 2008; p 355–371.